We are IntechOpen, the world's leading publisher of Open Access books Built by scientists, for scientists

6,900
Open access books available

185,000
International authors and editors

200M
Downloads

Our authors are among the

154
Countries delivered to

TOP 1%
most cited scientists

12.2%
Contributors from top 500 universities



WEB OF SCIENCE™

Selection of our books indexed in the Book Citation Index in Web of Science™ Core Collection (BKCI)

Interested in publishing with us?
Contact book.department@intechopen.com

Numbers displayed above are based on latest data collected.
For more information visit www.intechopen.com



Chapter 10

ESR and Magnetization Studies of Bi-manganites

Rajender Singh and Ramesh Ade

Additional information is available at the end of the chapter

http://dx.doi.org/10.5772/61936

Abstract

The electron spin resonance (ESR) and magnetization (M) studies of Bi-manganites were undertaken to understand the coexistence of various magnetic phases and their effect on charge ordering as a function of composition and temperature. The studies on several compositions of Bi-manganites reveal that the electronic phase separation (PS) is an intrinsic phenomenon in this system.

Keywords: Bi-manganites, ESR, magnetization, electronic phase separation

1. Introduction

The perovskite structure is represented by general composition ABO_3. Manganites belong to this family with A as trivalent (La^{3+}, Pr^{3+}, Bi^{3+}, etc.) and/or divalent (Ba^{2+}, Ca^{2+}, Sr^{2+}, etc.) ion and B as Mn ion. Manganites have a complex phase diagram and display interesting properties like colossal magnetoresistance (CMR) and giant magnetoresistance (GMR) [1–7]. These properties are the result of strong coupling between the charge, spin, and orbital degrees of freedom. The strength of this coupling depends on hydrostatic pressure [8, 9], magnetic and electric fields [10, 11], grain size [12, 13], and disorder created due to substitution at A-/B-site. The trivalent rare-earth ions doping of different sizes into the perovskite structure causes disorder in the sample due to change in chemical pressure, leading to the evolution of coexistence of various magnetic phases viz: paramagnetic (PM), ferromagnetic (FM), canted-antiferromagnetic (C-AFM), and antiferromagnetic (AFM). The phenomenon of phase separation (PS) has been proposed to explain the properties of manganites in view of inhomogeneities arising due to doping of the material. The PS can be electronic or structural. The electronic PS occurs when cluster formation takes place at nanometric level. The structural PS, which is due to disorder, can induce formation of up to micrometer-size clusters, which assist in percolation leading to first-order transitions [14–16]. The Griffiths Phase (GP) concept [17]

INTECH
open science | open minds

© 2016 The Author(s). Licensee InTech. This chapter is distributed under the terms of the Creative Commons Attribution License (http://creativecommons.org/licenses/by/3.0), which permits unrestricted use, distribution, and reproduction in any medium, provided the original work is properly cited.

has been used to explain the coexistence of FM and AFM domains in different types of manganites.

$Bi_{1-x}Ca_xMnO_3$ (BCMO) and $Bi_{1-x}Sr_xMnO_3$ (BSMO) manganites are insulating over the entire range of compositions with various phases [18–20]. The charge ordering temperature (T_{CO}) is 300–500 K for these materials, which is high compared to rare-earth materials. The charge ordering (CO) in these materials does not depend on the one electron bandwidth mechanism like in other manganites as it is due to highly polarizable $6s^2$ lone pair of Bi^{3+}ions.

In this chapter, we will review the recent work reported on these systems. The effect of substitution of various elements including transition elements at Bi- and Mn-site of these systems is reviewed. The study on various systems is considered to elucidate the intrinsic nature of PS phenomenon in these systems. In order to understand the evolution of various magnetic phases as a function of dopants at different sites and grain size; the following series of samples synthesized by solid-state (SS) or sol–gel (SG) methods are considered.

1. $Bi_{1-x}Ca_xMnO_3$ (x = 0.30–0.90) (BCMO)
2. $Bi_{0.5-x}Pr_xCa_{0.5}MnO_3$ (x = 0.0–0.50) (BPCMO)
3. La-doped Bi-manganites [$Bi_{0.7-x}La_xCa_{0.3}MnO_3$ (x = 0.07–0.70) and $Bi_{0.30}La_{0.37}Ca_{0.33}MnO_3$]
4. $Bi_{0.5}Ca_{0.5}Mn_{0.95}TE_{0.05}O_3$ (TE = V, Cu, and Zn)
5. $Bi_{0.5}Ca_{0.5}Mn_{0.95}TM_{0.05}O_3$ (TM = Ni, Fe, Co, and Cr)
6. $Bi_{0.55}Ca_{0.45}MnO_3$ and $Bi_{0.5}Ca_{0.5}MnO_3$ nanoparticles

The properties of the samples were studied using the following characterization techniques.

a. X-ray diffraction (XRD)
b. Scanning electron microscopy (SEM)
c. Energy dispersive x-ray spectroscopy (EDX)
d. Electron spin resonance (ESR)
e. Magnetization by vibrating sample magnetometer.

2. Electron spin resonance

There are two experimental techniques, namely magnetic resonance and inelastic neutron scattering, which can be used to describe the spin dynamics. Since double-exchange (DE) interaction mechanism is an intrinsic dynamical process, the investigation of spin dynamics and their static properties is crucial to study the magnetic properties of manganites. Although neutron scattering can provide information about magnetically ordered phases, but it has limitations in probing the spin dynamics of PM phases. The electron spin/paramagnetic resonance (ESR/EPR) is a sensitive technique which can help to understand the spin structure

and its dynamics in complex magnetic-ordered phases. This technique has been used by several scientists to study the spin dynamics of manganites. In the present work, the ESR technique is used to investigate various dynamical processes over a wide range of temperatures.

2.1. Origin of ESR in manganites

The Mn^{2+} ion (S = 5/2) is the most common ion detected by ESR. The Mn^{3+} ($3d^4$ with S = 2) exhibits a large zero-field splitting and strong spin-lattice relaxation and so unlikely to be ESR active [21]. The Mn^{4+} ions ($3d^3$ with S = 3/2) give an ESR signal usually at low temperatures. The manganese ions, Mn^{3+} and Mn^{4+}, are commonly seen in doped manganites. Theories suggesting that the two Mn^{3+} ions transforming into Mn^{2+} and Mn^{4+} ion pairs via thermally excited disproportionation were common [22–24]. It is generally accepted that manganites do not have, or have a very small ratio of, Mn^{2+} ions and hence do not contribute to the ESR signals exhibited by manganites. ESR signals obtained in La-based manganites have been attributed primarily to Mn^{4+} ions in an octahedral anion crystal electric field in ground state with a weak spin-lattice relaxation [25], which makes this ion ESR active even at higher temperatures [23]. Shengelaya et al. [25] attributes the ESR signal to Mn^{4+} in a system of three components such as Mn^{4+} ions, Mn^{3+} ions, and the lattice, and predicted an FM Curie–Weiss like behavior for the double-integrated line intensity, which is proportional to the static susceptibility arising from the FM couplings of the Mn^{4+} and Mn^{3+} magnetic subsystems [26]. But the ESR signals cannot be attributed to isolated Mn^{4+} ions. The origin of ESR signal observed in manganites has been assigned to some combinations or clusters of Mn^{3+}–Mn^{4+} ions coupled by a strong short-range FM–DE interaction [4, 27]. All the Mn ions are assumed to contribute to the ESR signal and the normalized double-integrated intensity (DI) is therefore proportional to the number of ESR centers and also a measure of ESR susceptibility (χ_{ESR}) [4, 28].

2.2. Theoretical background

The experimental ESR spectra (Fig. 1) was analyzed by Lorentzian expression given as

$$\frac{dP}{dH} = \frac{d}{dH} A \left(\frac{\Delta H}{4\left(H - H_0\right)^2 + \Delta H^2} + \frac{\Delta H}{4\left(H + H_0\right)^2 + \Delta H^2} \right) \quad (1)$$

where H_0 is the resonance field, ΔH is the linewidth, and A is a quantity proportional to the area under the curve which is related to the intensity of the signal [21, 29, 30]. The two terms in Eq. 1 describe the contribution from the clockwise and anticlockwise circularly polarized components of microwave radiation.

It was suggested [28] that when the ESR signals are intense near the critical point (Curie temperature, T_C), even for relatively small amount of samples, the ΔH depends strongly on the number of spins in the sample. Whenever large amount of samples are used, the sample size effects arise from overloading the cavity through magnetic losses [28, 31]. The ESR signals

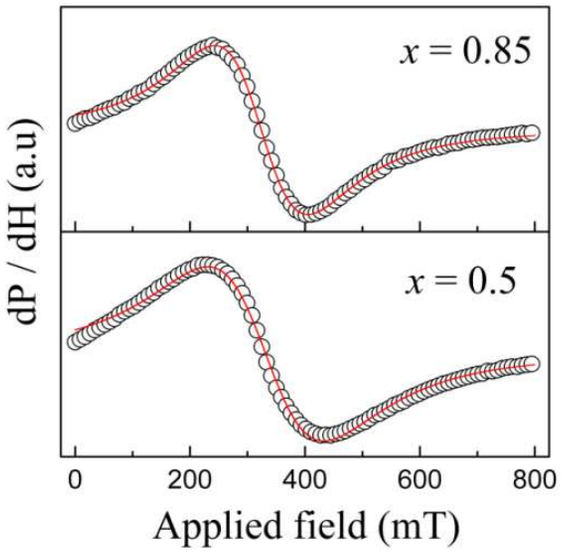


Figure 1. Lorentzian fit (solid red line) to the ESR spectra (open circles) of $Bi_{1-x}Ca_xMnO_3$ at 273 K [6].

remain Lorentzian as long as the magnetic losses are not large enough to drive the diode detector out of linearity [28]. When the sample is loaded in the cavity, at a fixed microwave frequency, ΔH can be given by the following expression

$$\Delta H^{obs} = \Delta H\left(1+b\right)^{1/2} \tag{2}$$

with

$$b = \frac{\left(4\pi/3\right)\eta Q_L \chi_{ESR}\omega}{\gamma \Delta H} \tag{3}$$

where χ_{ESR} is the static susceptibility corresponding to resonant species, η is the fitting factor, and Q_L is the loaded Q of the microwave cavity. Similarly, the changes in line intensity (I) also occur by size effects due to magnetic losses, and the expression for this can be given [28] as

$$I = \eta \chi_{ESR} \omega Q_L \left(1+b\right)^{-1/2} \tag{4}$$

These two equations (2) and (4) have certain limitations such as the value of b should be « 1. In addition to the sample dependent effects, frequency or applied field dependences of ΔH have also been reported [28, 32, 33]. Apart from the above-mentioned parameters, skin depth (δ) also affects the parameters I and ΔH of the ESR signal, and it is given by the expression

$$\delta = \left(\frac{\rho}{\mu_o \omega}\right)^{0.5} \tag{5}$$

where ρ is the resistivity of the sample measured at room temperature (RT), μ_o (= $4\pi \times 10^{-7}$ Vs/Am) is the permeability of free space, and ω (= $2\pi \times 9$ GHz) is the microwave frequency. The estimated values of δ are found to be in the range 0.2–1.5 mm, and it is larger than that of the size of samples [4]. In the present work, we have also taken care of cavity over loading problems. This ensures that the observed ESR signal intensity, ΔH, and resonance field (H_0) as a function of temperature are intrinsic in nature.

The study of magnetic properties of the samples with ESR technique is limited in the low temperatures due to its instrumental limitations. In order to support the ESR findings and to study the magnetic properties down to the temperature up to 5 K (from 350 K), the Quantum design Physical Property Measurement System (PPMS) was used. Magnetization as a function of temperature was measured in both zero field cooled (ZFC) and field cooled (FC) by applying a field of 500 Oe.

2.3. Studies on $Bi_{1-x}Ca_xMnO_3$ (x = 0.30–0.90)

Figure 2 depicts the Rietveld refinement of XRD pattern for the sample with x = 0.65. With the refinement, XRD data are well reproduced with *Pnma* space group orthorhombic structure of all the samples except the sample with x = 0.30. Using the refined parameters crystal structure is generated for all the samples, as shown in Fig. 3 for $Bi_{0.35}Ca_{0.65}MnO_3$ which is representative of all the samples. With increase in Ca content, decrease in unit cell volume is observed. This is ascribed to lower ionic radii of Ca^{2+} (1.12 Å) than that of Bi^{3+} (1.24 Å) ion.

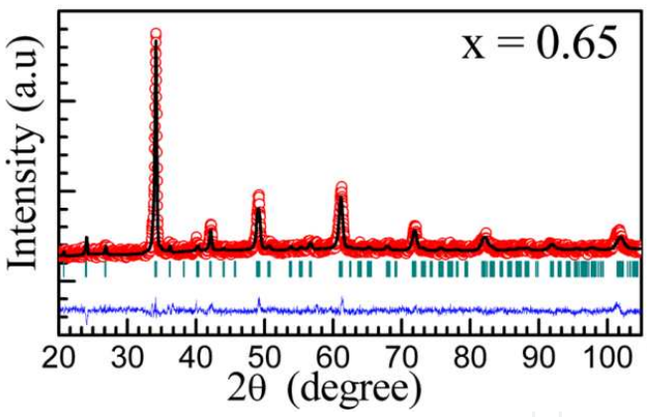


Figure 2. Rietveld refinement of the XRD data of $Bi_{1-x}Ca_xMnO_3$.

Figure 4 shows *DI* of ESR signal as a function of temperature. For samples with $0.40 \le x \le 0.80$, as the temperature decreases from high temperature (453K), *DI* increases and reaches its maximum, which is assigned as charge ordering temperature (T_{CO}) [5]. Below T_{CO}, *DI* decreases, evidencing the existence of AFM correlations and reaches a minimum and then it increases with further decrease in temperature for samples with $0.65 \le x \le 0.80$. For x = 0.30 sample, a weak T_{CO} is observed. For x = 0.85 and 0.90 samples, no T_{CO} is observed. For x = 0.85 and 0.90 samples, on cooling from high temperature, *DI* increases gradually. For $0.30 \le x \le 0.80$ samples,

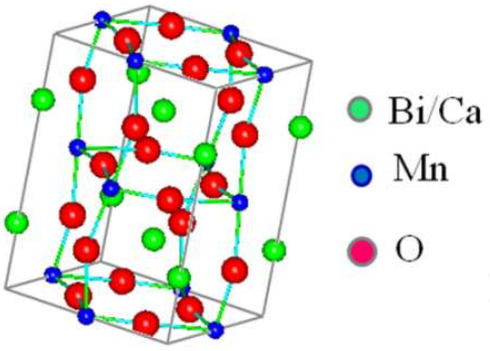


Figure 3. Crystal structure of $Bi_{0.35}Ca_{0.65}MnO_3$.

sharp decrease in *DI* below the temperature ~126–150 K is assigned as the temperature at which onset of long-range AFM ordering takes place, that is, Neel temperature (T_N).

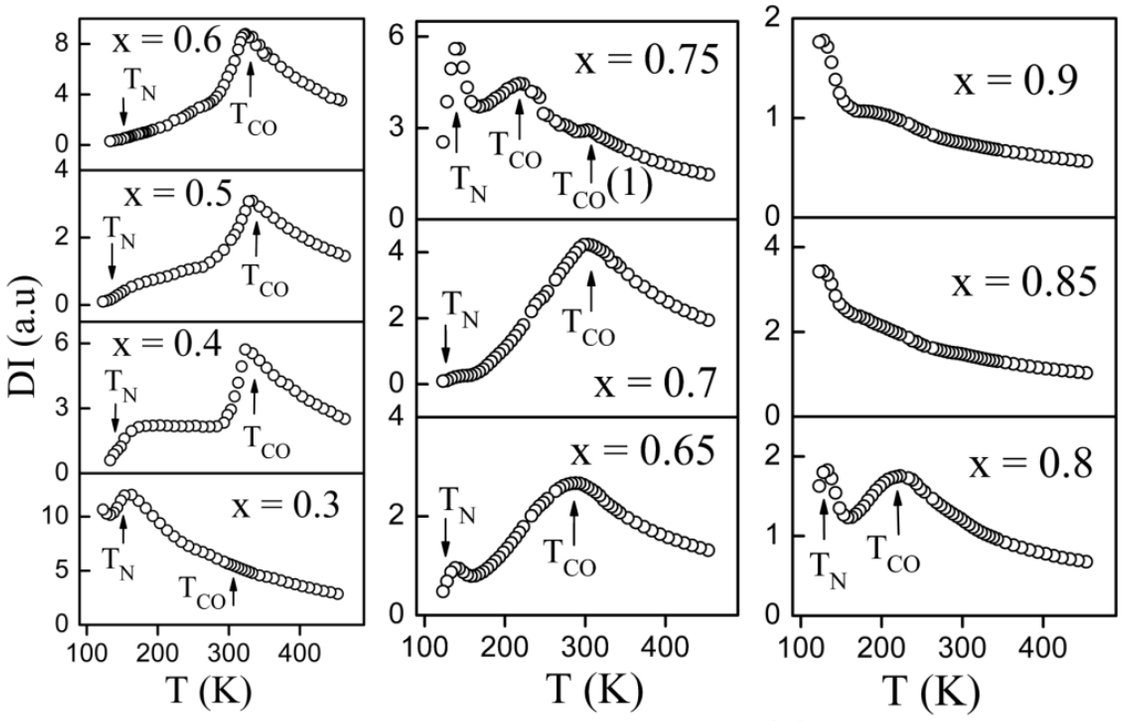


Figure 4. *DI* vs *T* plots of $Bi_{1-x}Ca_xMnO_3$ samples.

The 1/*DI* vs *T* plots for various samples are shown in Fig. 5. The linear fit in the high-temperature range is as per Curie–Weiss law [5]. The positive intercept on the x-axis in the temperature range $T > T_{CO}$ for samples with $0.30 \leq x \leq 0.80$, indicates the existence of FM–DE correlations. The charge ordering transition of $0.65 \leq x \leq 0.80$ samples is smeared compared to what is observed for samples with $x \leq 0.60$. The CO transition at 303 K is weak for sample with $x = 0.75$. The existence of Bi-rich CO phase, a chemical phase separation in the samples, with $x = 0.75$, 0.70, and 0.65 may be the reason for this. The upward and downward trend in 1/*DI* vs *T* plots

http://dx.doi.org/10.5772/61936

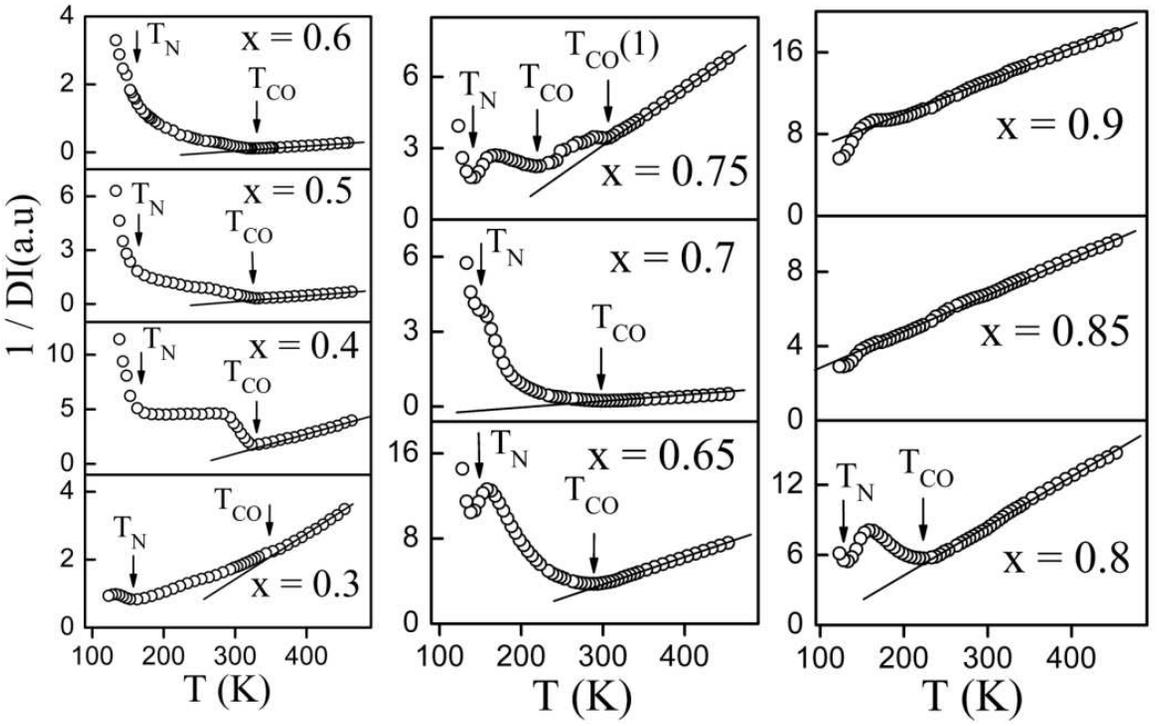


Figure 5. 1/*DI* vs *T* plots of $Bi_{1-x}Ca_xMnO_3$ samples. Ref. [5]

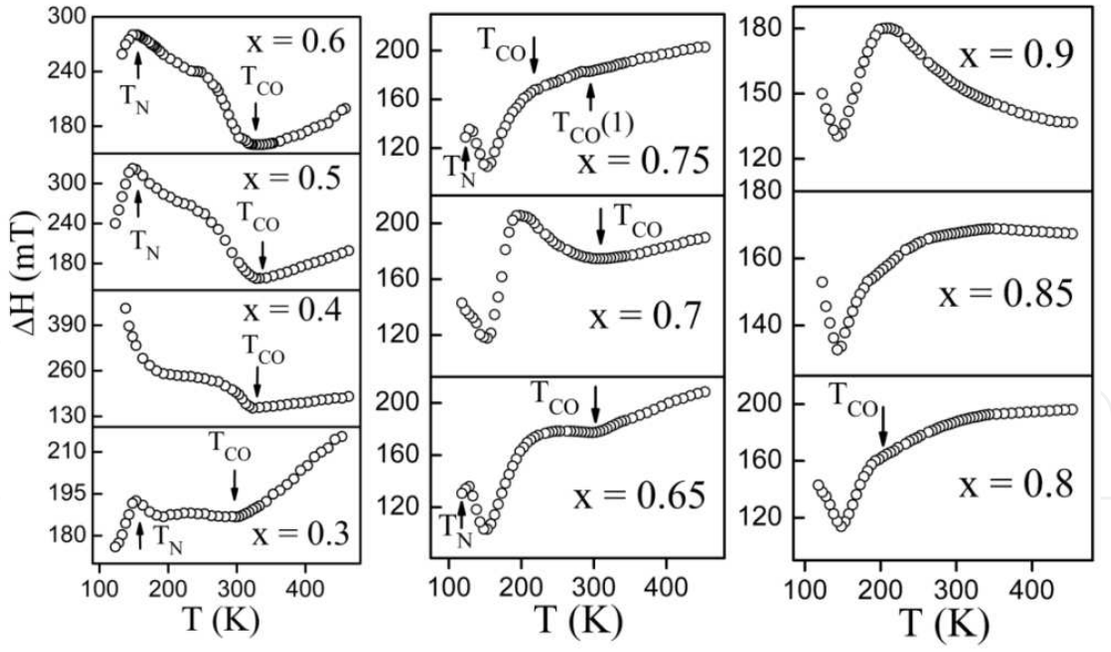


Figure 6. Δ*H* vs *T* plots of $Bi_{1-x}Ca_xMnO_3$ samples. Ref. [5].

below T_{CO} is an indication whether AFM or FM interactions dominate in the respective temperature range [5]. The minima in these plots indicate the onset of CO or AFM ordering. For samples with x = 0.65, 0.75, and 0.80, 1/*DI* vs *T* plots show a broad peak at ~160 K, which

is attributed to C-type AFM correlations. The down turn behavior of 1/*DI* in the temperature range below 148 K for the samples with $x = 0.85$ and 0.90 can also be explained in view of short-range ordering of FM clusters in PM matrix as per Griffiths theory. The negative intercept on the x-axis for samples with $x = 0.85$ and 0.90 indicates dominant AFM-superexchange (SE) interactions above 150 K. Below 150 K, localized FM correlations dominate [4–6].

Figure 6 shows ΔH as a function of temperature. For samples with $x \geq 0.65$, ΔH shows prominent minima at ~150 K. The ESR signal persists only for a few degrees below 150 K for all the samples and then it disappears indicating the onset of long-range AFM state (T_N). ΔH increases linearly with increase in temperature in the temperature range $T \geq T_{CO}$. ΔH saturates with increase in temperature as T_{CO} decreases with increase in x. This effect is clearly seen for sample with $x = 0.8$. ΔH increases with decrease in temperature for the sample with $x = 0.90$, indicating the strengthening of AFM interactions with lowering of temperature.

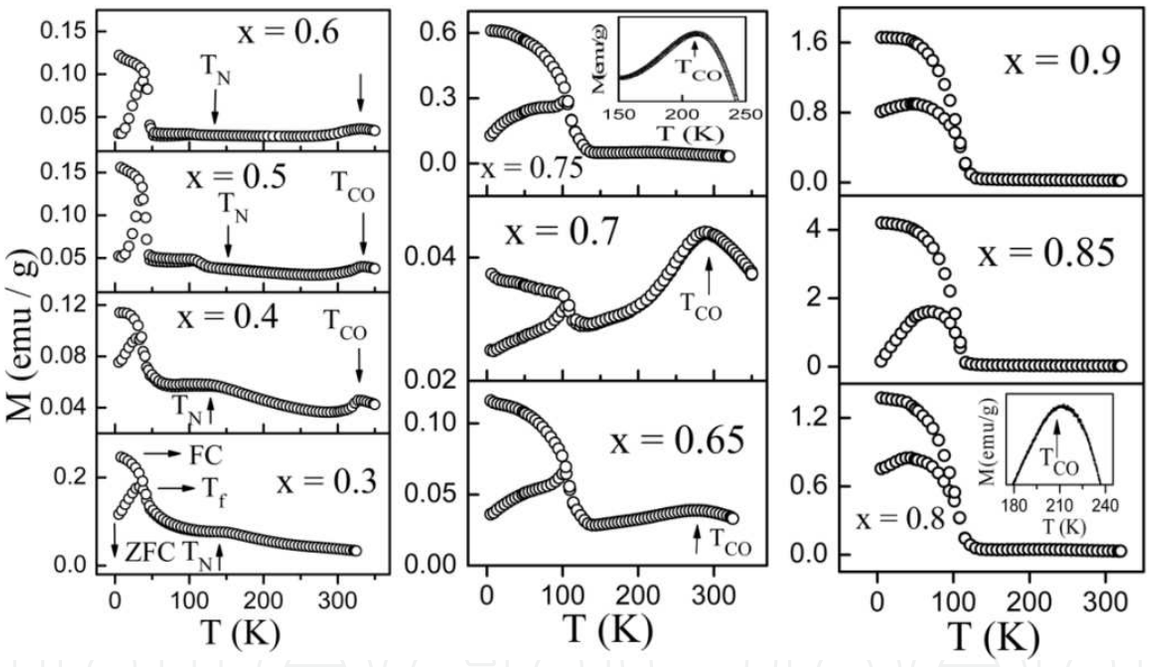


Figure 7. *M* vs *T* plots of $Bi_{1-x}Ca_xMnO_3$ samples.

Figure 7 shows magnetization vs temperature (*M* vs *T)* plots for various samples. As the temperature decreases from 350 K, both ZFC and FC curves show a peak at T_{CO} for samples with $0.30 \leq x \leq 0.80$. *M* decreases slightly on further decrease in temperature. The broad maximum at ~150 K observed for samples with $x \leq 0.50$ represents long-range AFM order [6]. The sharp rise in *M* for samples with $x \leq 0.60$ at ~50 K is related to the spin-glass (SG) or cluster-glass (CG) transitions which arises due to competition between FM interaction in $BiMnO_3$-type clusters and AFM coupling in clusters in which Mn^{3+} orbits are frozen in random orientations [6]. For these samples, *M* vs *T* plots in ZFC mode show a peak in *M* at spin freezing temperature (T_f). A small peak in *M* at ~120 K observed for sample with $x = 0.50$ is ascribed to field-induced

http://dx.doi.org/10.5772/61936

spin canting in the AFM phase aided by the spontaneous canting moment [6]. The trend and the conclusions drawn from $1/\chi$ vs T (not shown) and $1/DI$ vs T plots are similar.

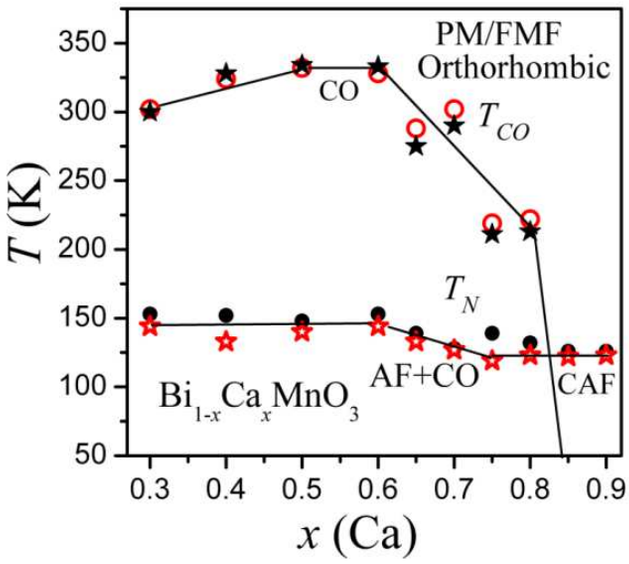


Figure 8. Phase diagram of BCMO system. Open circles (T_{CO}) and closed circles (T_N) are from ESR data and closed stars (T_{CO}) and open stars (T_N) from magnetization data [6]

Figure 8 shows the estimated values of T_{CO} and T_N from the ESR and magnetization data for $Bi_{1-x}Ca_xMnO_3$. The magnetic phase in the temperature range $T > T_{CO}$ is dominated by FM–DE interactions for samples with $0.30 \leq x \leq 0.80$. The PM–AFM transition at ~150 K coexists with PM to C-AFM transition at ~120 K for samples with $0.50 \leq x \leq 0.80$, whereas for samples with $x = 0.85$ and 0.90, only PM to C-AFM transition is observed.

2.4. Studies on $Bi_{0.5-x}Pr_xCa_{0.5}MnO_3$ ($0.0 \leq x \leq 0.50$) manganites

The XRD study of the $Bi_{0.5-x}Pr_xCa_{0.5}MnO_3$ ($0.0 \leq x \leq 0.50$) samples [34] confirms the single-phase orthorhombic nature with *Pnma* space group. A sharp decrease in the unit cell volume is observed as Pr content increases from $x = 0.0$ to 0.05. However, the unit cell volume increases steadily with further increase in Pr content from 0.05 to 0.50. The Bi^{3+} has effective ionic size of 1.170 or 1.24 Å depending on whether the $6s^2$ lone pair character is constrained or dominant, respectively [34]. The higher cell volume of undoped sample may be due to the strengthened dominant lone pair character of Bi^{3+} ion, whereas the sharp drop in the cell volume for sample with $x = 0.05$ indicates that the constrained effect of the $6s^2$ lone pair becomes strong due to Pr doping. The increase in cell volume for samples with $x > 0.05$ indicates that the constrained effect of the lone pair maintains the Bi^{3+} ionic size at 1.170 Å, that is, smaller than Pr^{3+} ionic size (1.179 Å).

The temperature dependence of ΔH of ESR signal is shown in Fig. 9. As temperature decreases from high temperature (453 K), ΔH decreases and reaches a minimum value at T_{CO}. At ~200 K, ΔH decreases sharply and reaches a minimum at 130, 150, and 160 K for samples with $0.05 \leq x \leq 0.15$, $0.20 \leq x \leq 0.40$, and $x = 0.50$, respectively. These minima indicate the existence of FM

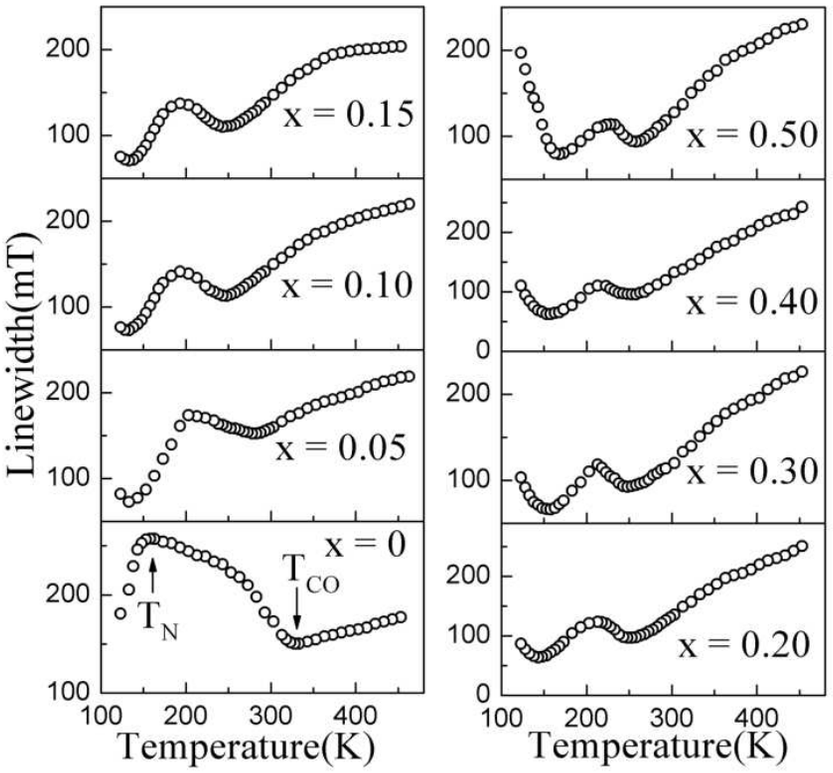


Figure 9. Linewidth versus Temperature plots of $Bi_{0.5-x}Pr_xCa_{0.5}MnO_3$ samples.

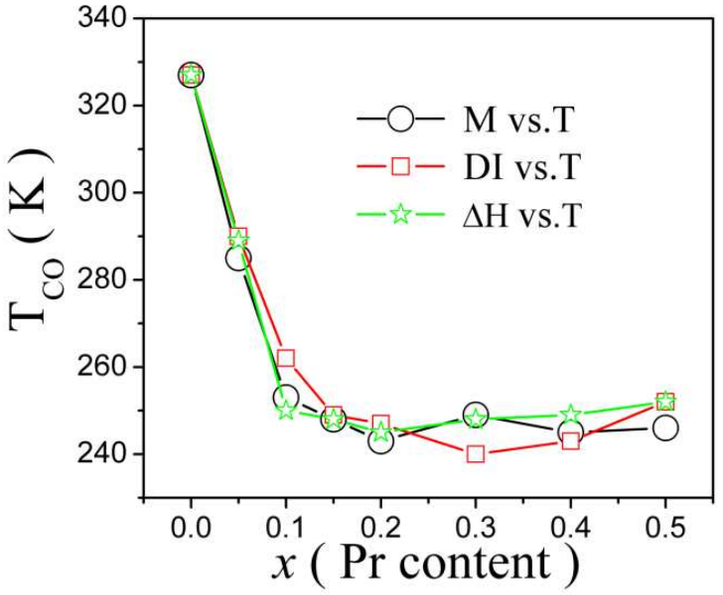


Figure 10. T_{CO} versus x of $Bi_{0.5-x}Pr_xCa_{0.5}MnO_3$ samples.

magnetic clusters embedded in the AFM matrix. Further, decrease in temperature leads to increase in ΔH due to the evolution of canted-AFM (C-AFM) phase.

http://dx.doi.org/10.5772/61936

The value of T_{CO}, as a function of Pr content (Fig. 10), estimated from ESR data matches quite well with those estimated from magnetization data analysis. T_{CO} decreases as x increases from 0.0 to 0.20 and becomes independent of doping content with further increase in x. For samples with $0.0 \leq x \leq 0.15$, T_{CO} decreases and Curie–Weiss temperature (θ_C) increases with increase in Pr doping.

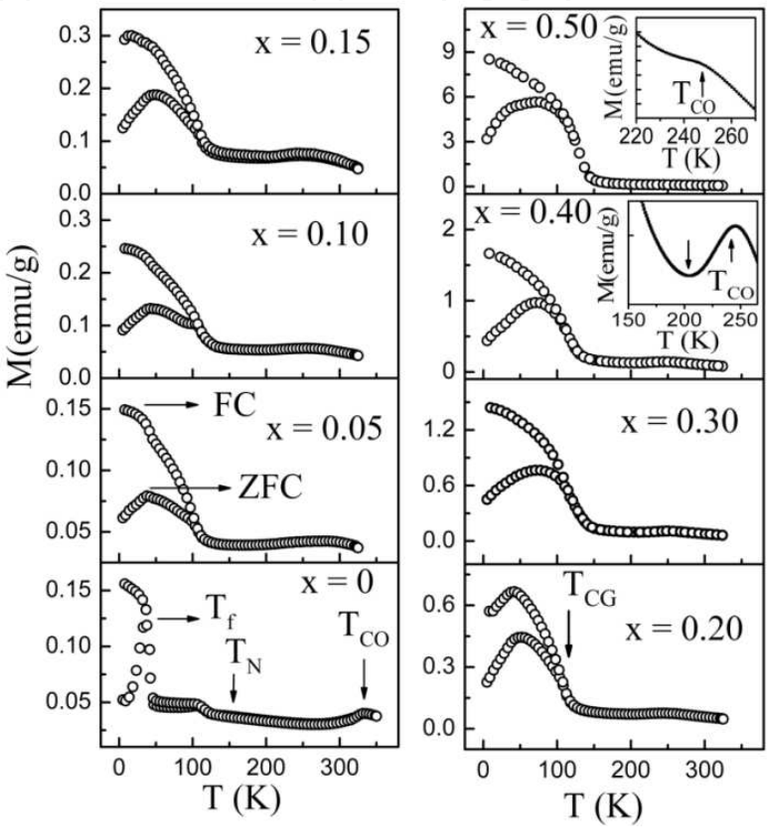


Figure 11. M versus T plots of $Bi_{0.5-x}Pr_xCa_{0.5}MnO_3$ samples sizes measured under the applied static field of 500 Oe.

The sharp rise in M (Fig. 11) value below 45 K for undoped sample and below 115 K for doped samples is observed, which is characteristic of FM-cluster glass (CG) behavior. The temperature T_f is called spin-freezing temperature. Below this temperature, M in ZFC mode decreases due to the competition between the evolving FM and AFM interactions, whereas M in FC mode continuously increases with decreasing temperature.

2.5. Studies on La-doped Bi-manganites

The base compound, $Bi_{0.7}Ca_{0.3}MnO_3$, has monoclinic structure, and the details are given in section 2.3, whereas the La-doped Bi-manganites, $Bi_{0.7-x}La_xCa_{0.3}MnO_3$ (x = 0.07, 0.14, 0.28, 0.35 and 0.7), have cubic structure. The unit cell volume increases with increasing La content.

Figure 12 shows the ESR spectra for x = 0.07 and 0.70 samples at some selected temperatures. For all samples, the ESR spectra above a particular temperature (~260–270 K) show a single resonance line at resonance field of 325 mT, which is characteristic of the existence of PM phase.

Below this temperature, FM correlations evolve in the PM matrix as indicated by the appearance of a shoulder (shown with '↓1') in the low-field region of the ESR signal. This shoulder can be assigned to a low-moment state. With further decrease in temperature, FM correlations grow at the expense of PM interactions, as a result of which a complete PM–FM transition occurs below ~180 K. This is indicated by the shift of the shoulder toward further lower-field region (shown with '↓2'). The data indicate development of a high-moment state as temperature decreases.

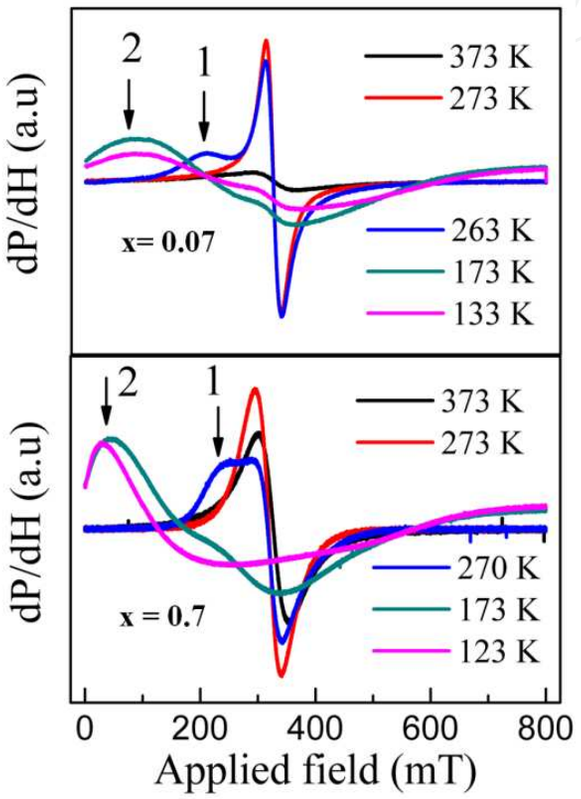


Figure 12. ESR spectra of $Bi_{0.7-x}La_xCa_{0.3}MnO_3$ (x = 0.07, 0.7).

Figure 13 shows M vs T plots of all the samples. M increases with increasing La content. The spin or cluster glass behavior of Bi- and La-containing samples is similar to that of $Bi_{1-x}Ca_xMnO_3$ ($x \leq 0.6$) system [6]. The samples show the coexistence of PM–FM phases over a wide temperature range. The estimated T_C, θ_C, and the temperature at which ΔH becomes minimum (T_{min}) increase with increase in La content.

The critical behavior of $Bi_{0.30}La_{0.37}Ca_{0.33}MnO_3$ (orthorhombic structure with *Pnma* space group) manganite at the critical point, where the system undergoes phase transition from PM to FM state, is investigated by using modified-Arrott plots (Fig. 14), Kouvel-Fisher method (Fig. 15), and critical isotherm analysis [35].

The sample shows second-order phase transition near the critical point [36]. The estimated critical exponents are close to as per the prediction by mean-field theory (MFT).

http://dx.doi.org/10.5772/61936

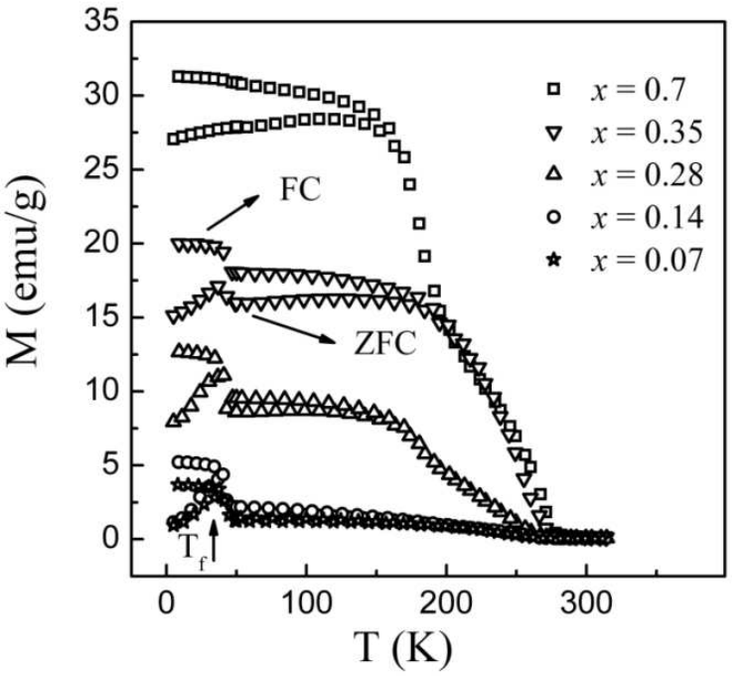


Figure 13. *M* versus *T* plots of $Bi_{0.7-x}La_xCa_{0.3}MnO_3$ samples measured under the applied static field of 500 Oe.

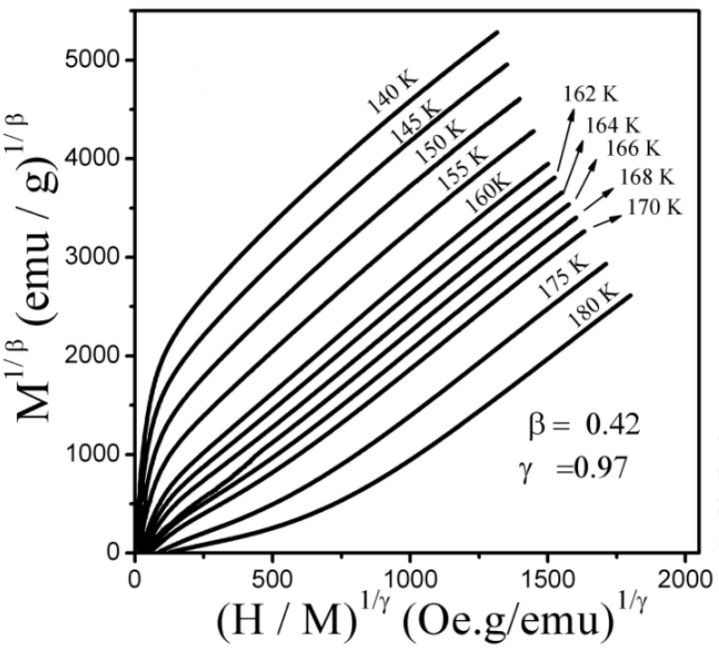


Figure 14. Modified Arrott plots of $Bi_{0.30}La_{0.37}Ca_{0.33}MnO_3$.

Using scaling equation,

$$M(H,\varepsilon) = \varepsilon^{\beta} f_{\pm}\left(H / \varepsilon^{\beta+\gamma}\right) \tag{6}$$

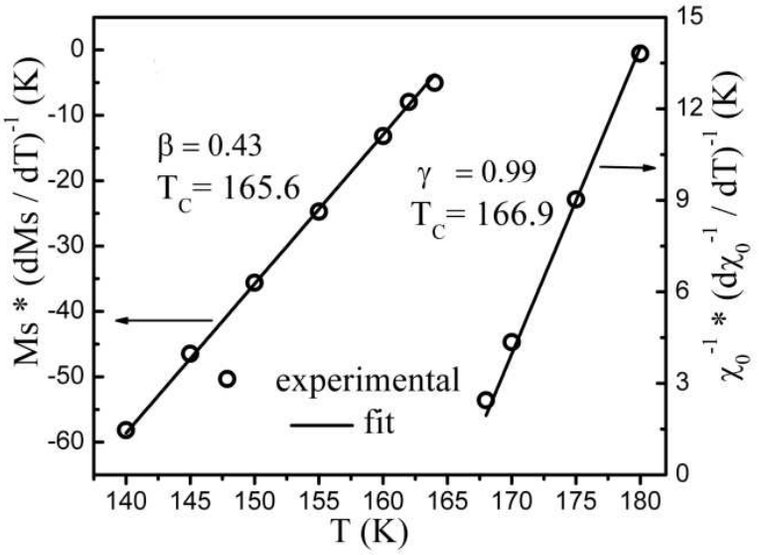


Figure 15. Kouvel-Fisher plots of $Bi_{0.30}La_{0.37}Ca_{0.33}MnO_3$.

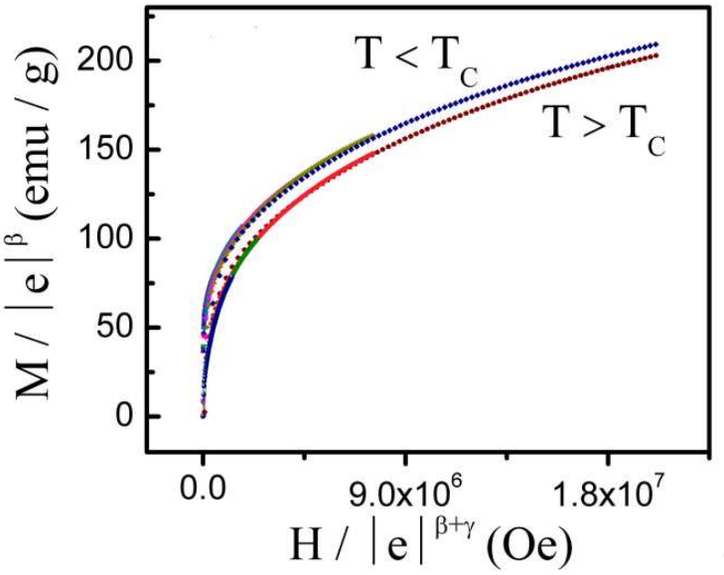


Figure 16. Scaling plots below and above T_C using the critical exponents determined from Kouvel–Fisher method of $Bi_{0.30}La_{0.37}Ca_{0.33}MnO_3$.

where f_+ for $T > T_C$ and f_- for $T < T_C$ are regular functions [35], we have plotted as shown in Fig. 16. There are two curves, one above the T_C and the other one below T_C, in agreement with the scaling theory. This indicates that the calculated critical exponents are reliable.

$Bi_{1-x}Ca_xMnO_3$ (BCMO) exhibits charge ordering property in the composition range $0.30 \le x \le 0.80$, which is related to first-order transition [3–6]. At critical point, $La_{1-x}Ca_xMnO_3$ (LCMO) manganite shows first-order transition in the composition range $0.30 \le x \le 0.40$ and second-order transition in the composition range $0.18 \le x \le 0.25$ and $0.40 \le x \le 0.48$ [37–39], whereas the present $Bi_{0.30}La_{0.37}Ca_{0.33}MnO_3$ sample also exhibits second-order transition which is similar

to $La_{0.7}Sr_{0.3}MnO_3$ (LSMO) [40]. In the present system, due to La^{3+} doping, the average A-site ionic radius increases, as in the case of Sr^{2+}-doped La-manganite. The increased average A-site radius might be responsible for the observed second-order phase transition.

The ESR and magnetization studies on La-doped Bi-manganites reveal that the La-doping increases *M* as well as various transition temperatures describing the evolution of various magnetic phases. These changes are ascribed to the difference in ionic radii of Bi^{3+} and La^{3+} ions and the variations in $6s^2$ lone pair character of Bi^{3+} ions with La-doping.

2.6. Comparative studies on fixed doping level of transition element (TE = V, Cu and Zn) at Mn-site in $Bi_{0.5}Ca_{0.5}MnO_3$ system

XRD data analysis indicates that all the samples possess orthorhombic structure [41]. The difference between *a* and *b* lattice parameters decreases, and the *c* lattice parameter increases with doping. The change in the lattice parameters with doping confirms that the dopants are substituted at the Mn-site [41].

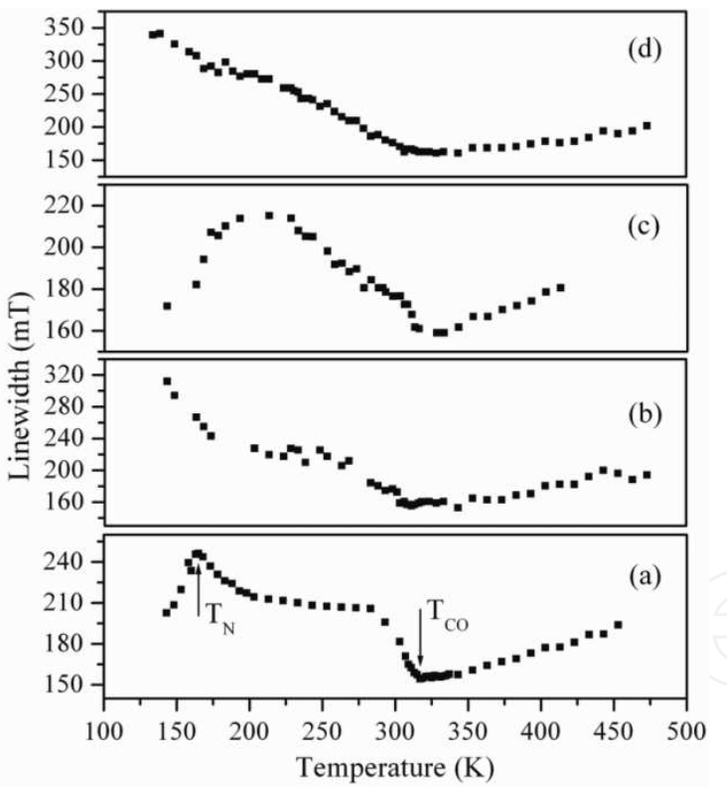


Figure 17. Linewidth versus temperature plots for $Bi_{0.5}Ca_{0.5}Mn_{0.95}TE_{0.05}O_3$ (a) undoped and doped samples with TE (b) V (c) Cu and (d) Zn [41]

ESR (Fig. 17) studies on $Bi_{0.5}Ca_{0.5}Mn_{0.95}TE_{0.05}O_3$ with TE = V, Cu, and Zn as a function of temperature and composition show a strong interplay between FM and AFM interactions. FM and AFM phases coexistence in the temperature range $T_{CO} > T > T_O$ for all the samples. In the temperature range $T > T_{CO}$, all samples show FM-dominated interactions in PM state.

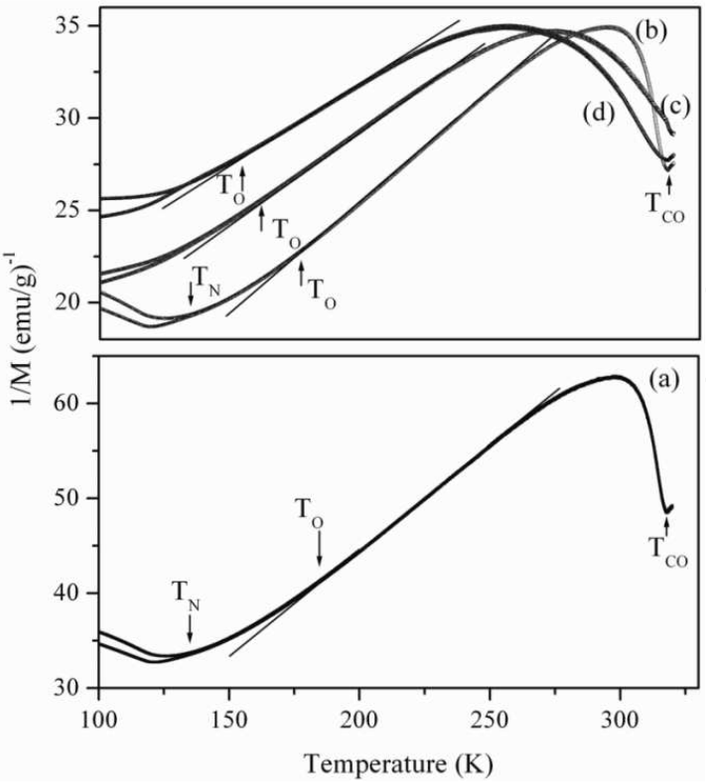


Figure 18. 1/*M* versus *T* plots for $Bi_{0.5}Ca_{0.5}Mn_{0.95}TE_{0.05}O_3$ (a) undoped and doped samples with TE (b) V (c) Cu (d) Zn [41]

The magnetization data in Fig. 18 supports the ESR observations. The estimated values of θ_C in the temperature range $T_{CO} > T > T_O$ (Fig. 18) are 5, –7, –93, and –172 K for undoped, V-, Cu-, and Zn-doped samples, respectively. The changes in magnetic properties of BCMO system with TE doping at Mn-site are due to the electronic nature of the dopants [41].

2.7. Comparative studies on fixed doping level of transition metals (TM = Ni, Fe, Co, and Cr) at Mn-site in $Bi_{0.5}Ca_{0.5}MnO_3$ system

All the samples have orthorhombic structure [42]. The Mn replacement by TM was confirmed by change in the lattice parameters with respect to lattice parameters of undoped one. This effect is weak for Co-doped sample compared to Fe-, Cr-, and Ni-doped samples. The peak widths of Cr-doped XRD pattern are essentially broader than for other TM-doped samples. It can be due to the non-homogeneous Cr-doped phase. It can also be due to smaller crystallite size in Cr-doped sample than other samples [42].

The ESR (Fig. 19) and magnetization (Fig. 20) data on the present BCMO and BCMTMO samples show that the FM correlations dominate in the temperature region $T > T_{CO}$. In the temperature range, $T_{CO} > T > T_O$, FM and AFM coexist for the undoped, Ni- and Fe-doped samples. The 3d TM doping melts the charge ordering and AFM ordering. The effect of Fe, Co, and Cr doping is same and stronger compared to Ni. This suggests that the dopants modify the interaction between Mn ions and possibly alter the band structure of the material instead of participating directly in the magnetic interaction mechanisms [42].

http://dx.doi.org/10.5772/61936

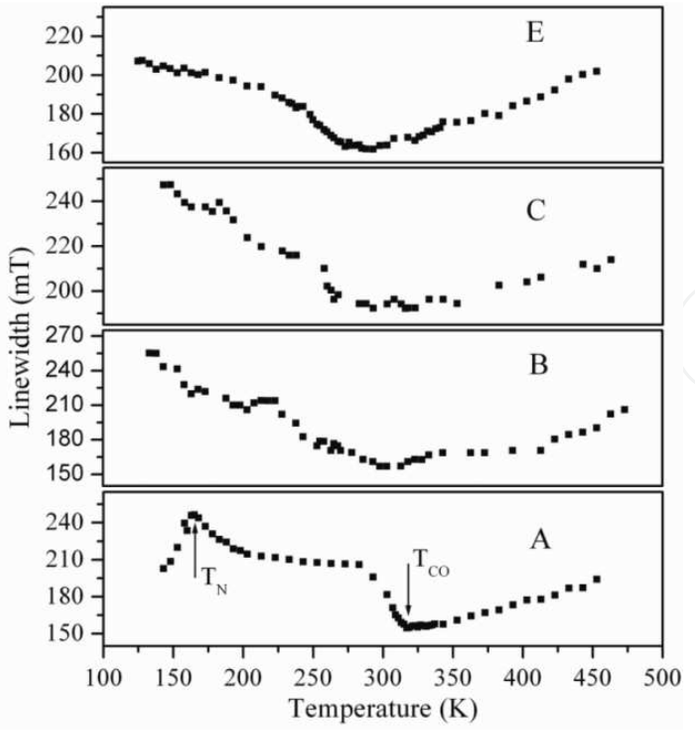


Figure 19. Linewidth versus Temperature plots for A-$Bi_{0.5}Ca_{0.5}MnO_3$ and $Bi_{0.5}Ca_{0.5}Mn_{0.95}TM_{0.05}O_3$ (TM = B-Ni, C-Fe and E-Cr)

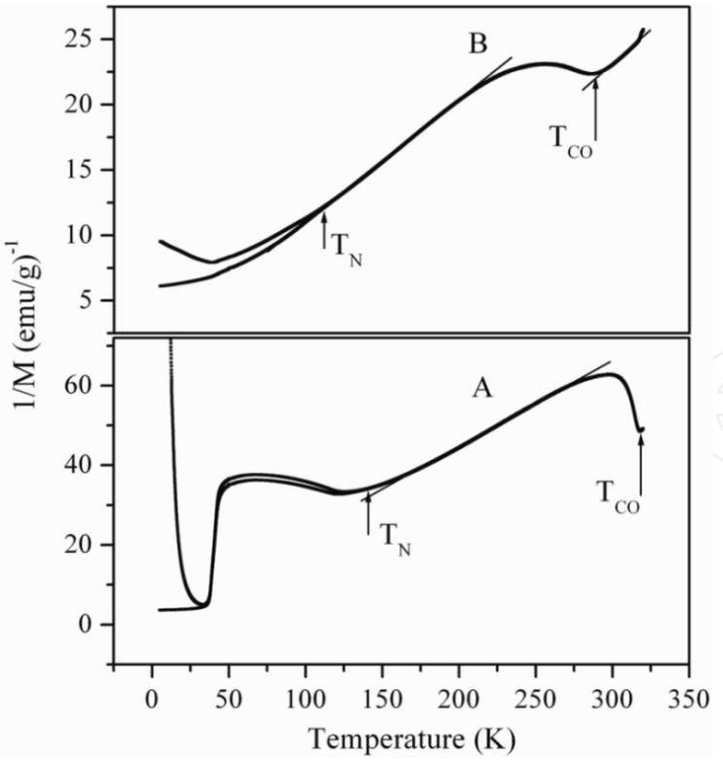


Figure 20. 1/*M* versus *T* plots for doped $Bi_{0.5}Ca_{0.5}Mn_{0.95}TM_{0.05}O_3$ (A-undoped, B-TM = Ni)

2.8. Studies on nanoparticles

The comparative ESR studies (Fig. 21) on bulk and nanometer-size (grain size 21 and 15 nm) samples of $Bi_{0.55}Ca_{0.45}MnO_3$ show that T_{CO} decreases from 313 to 306 K as sample grain size changes from bulk to 15 nm. The T_N value remains around 153 K for all the samples. In Fig. 21, the solid lines are as per Curie–Weiss law. Above $T_{CO,}$ the positive intercepts on the x-axis indicate the dominant FM correlations. In the temperature range, $T_{CO} > T > T_N$, the domains of FM and AFM spin correlations coexist [43]. The FM phase volume decreases, and the transitions become sharp with decrease in grain size [43].

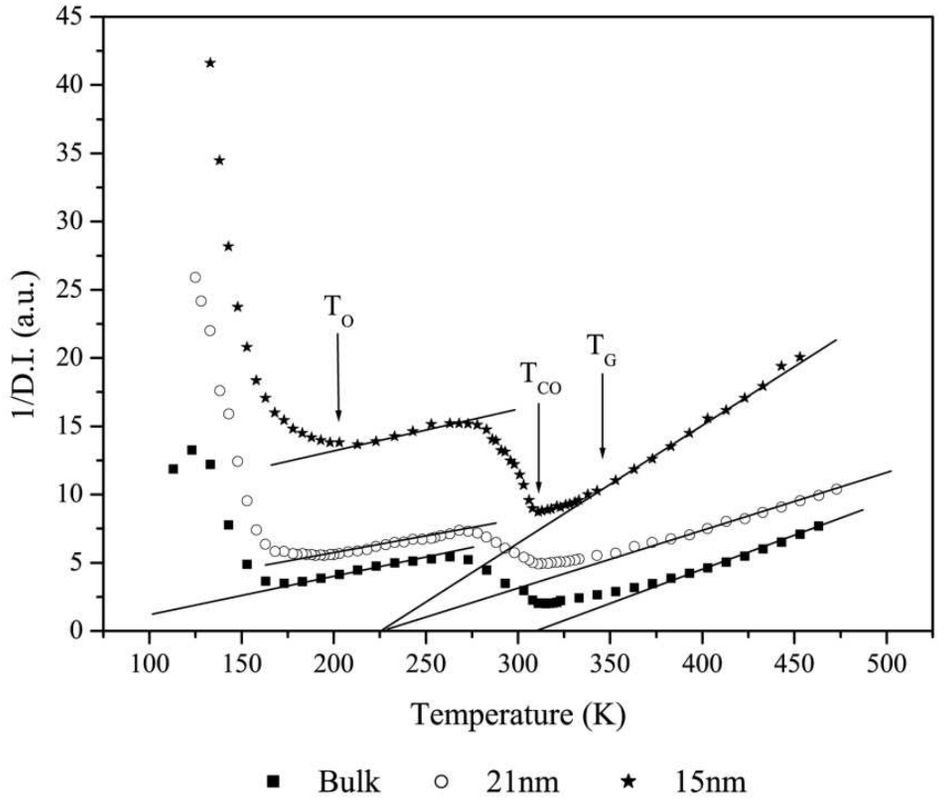


Figure 21. 1/*DI* versus *T* plots for the samples Bulk sample (filled squares), 21 nm nanoparticles (open circles) and 15 nm nanoparticles (filled stars).

The ESR data have been explained [43] in view of the Griffith's phase theory [9]. Griffith's theory suggests that above T_G large FM clusters form. Below T_G, smaller-sized clusters form, reducing the average size of the FM clusters. In Fig. 21, nonlinear decrease of *1/DI* with decrease in temperature indicates existence of FM cluster in a PM matrix. In the temperature range, $T_{CO} > T > T_N$, orbital ordering sets in, bringing about long-range AFM ordering. In this temperature range, the Mn spins do not completely undergo OO and hence there is a coexistence of FM and AFM phases.

The effect of grain size on the properties of $Bi_{0.5}Ca_{0.5}MnO_3$ manganite samples synthesized by SG method is also studied. The samples with grain size (27, 450, and 1080 nm) were obtained

http://dx.doi.org/10.5772/61936

by appropriate heat treatment schedule. The magnetic behavior of samples with grain size 450 and 1,080 nm is similar to that of bulk sample described in (section 2.3), whereas for sample with GS 27 nm, the long-range charge ordering and AFM ordering transitions are suppressed (Fig. 22). Magnetization results (Fig. 23) also support the ESR findings.

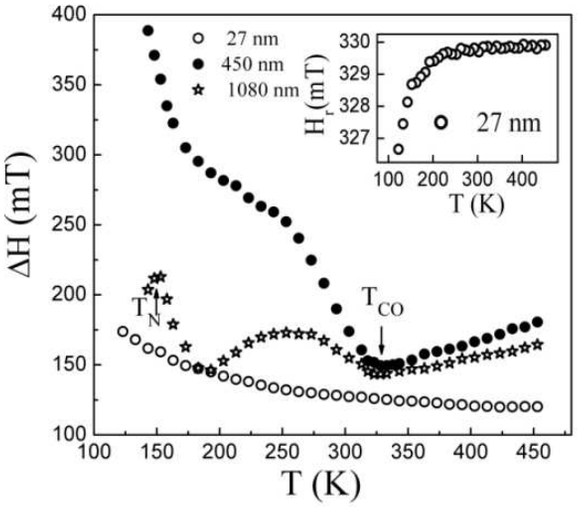


Figure 22. ΔH versus T plots of $Bi_{0.5}Ca_{0.5}MnO_3$ sample with different grain sizes. Inset shows H_r versus T plot for 27 nm sample.

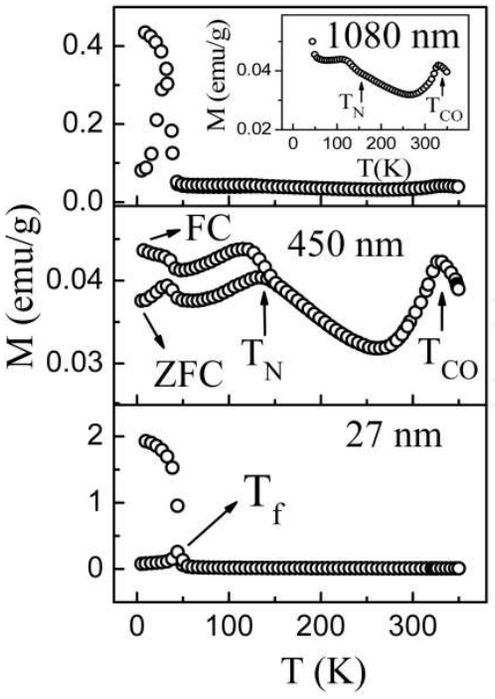


Figure 23. M versus T plots of $Bi_{0.5}Ca_{0.5}MnO_3$ sample with different grain sizes measured under the applied field of 500 Oe.

For these samples, M in FC mode increases with decreasing temperature. However, the ESR and magnetization results reveal that even for sample with GS 27 nm the AFM correlations still exist in the form of short-range order. The shift in FM–CG transition and T_f toward higher temperature and the sharp rise in M below 50 K for sample with GS 27 nm are observed. The evolving different magnetic correlations with decrease in GS are ascribed to increase in surface-to-volume ratio of grains.

3. Conclusions

The ESR and M studies of Bi-manganites of various compositions synthesized by SS or SG methods are reviewed. The effect of substitution of divalent (Ca^{2+}) and trivalent (Pr^{3+} and La^{3+}) cations at Bi-site and partial replacement of Mn by transition elements on the structure and magnetic properties of these materials is reviewed. The effect of grain size on the evolution of various magnetic interactions is also described. The study on various systems is useful in understanding the evolution of various magnetic phases as a function of composition and temperature. The studies on several compositions of Bi-manganites reveal that electronic phase separation is an intrinsic phenomenon in this system.

Acknowledgements

Ramesh Ade would like to thank the award of UGC-(JRF+SRF) from CSIR India.

Author details

Rajender Singh* and Ramesh Ade

*Address all correspondence to: rssp@uohyd.ernet.in

School of Physics, University of Hyderabad, Central University, Hyderabad, Telangana, India

References

[1] Jonker G H and Van Santen J H. Ferromagnetic compounds of manganese with perovskite structure. Physica, 1950; XVI: 337–349.

[2] Wollan E O and Koehler W C. Neutron diffraction study of the magnetic properties of the series of perovskite-type compounds [(1–*x*)La, *x*Ca]MnO_3. Physical Review, 1955; 100: 545–563.

[3] Kurian J and Singh R. Electron spin resonance study of $Bi_{(1-x)}Ca_xMnO_3$, Journal of Applied Physics, 2008; 103: 07F707(1)–07F707(3).

[4] Kurian J and Singh R. Electron spin resonance and resistivity studies of charge-ordered $Bi_{1-x}Ca_xMnO_3$. Journal of Physics D: Applied Physics, 2008; 41: 215006–215015.

[5] Ramesh A and Singh R. Electron spin resonance studies of $Bi_{1-x}Ca_xMnO_3$ ($x \geq 0.65$). IEEE Transactions on Magnetics, 2012; 48: 4562–4565.

[6] Ramesh A and Singh R. Electron spin resonance and magnetization studies of $Bi_{1-x}Ca_xMnO_3$. Physica B, 2014; 448: 273–276.

[7] Uehara M, Mori S, Chen C H and Cheong S-W. Percolative phase separation underlies colossal magnetoresistance in mixed-valent manganites. Nature (London), 1999; 399: 560–563.

[8] Cui C and Tyson T A. Pressure effects on charge, spin, and metal-insulator transitions in the narrow bandwidth manganite $Pr_{1-x}Ca_xMnO_3$. Physical Review B, 2004; 70: 094409(1)–094409(8).

[9] Wang X, Cui Q, Pan Y, Gao W, Zhang J and Zou G. High pressure effects on the Jahn–Teller distortion in perovskite $La_{0.5-x}Bi_xCa_{0.5}MnO_3$. Journal of Alloys and Compounds, 2001; 321: 72–75

[10] Tomioka Y, Asamitsu A, Kuwahara H, Moritomo Y and Tokura Y. Magnetic-field-induced metal-insulator phenomena in $Pr_{1-x}Ca_xMnO_3$ with controlled charge-ordering instability. Physical Review B, 1995; 53: R1689–R1692.

[11] Yang C P, Chen S S, Guo D H, Wang H, Rao G H, Morchshakov V and Barner K. Electrical-field-induced order transitions in Sr-doped manganite perovskites. Journal of Alloys and Compounds, 2009; 467: 54–60.

[12] Zhang T and Dressel M. Grain-size effects on the charge ordering and exchange bias in $Pr_{0.5}Ca_{0.5}MnO_3$: The role of spin configuration. Physical Review B, 2009; 80: 014435(1)–014435(9).

[13] Rozenberg E, Shames A I and Auslender M. Nanometer sized effects on magnetic ordering in La–Ca manganites, probed by magnetic resonance. Nanoscience and Nanotechnology Letters, 2011; 3: 531–540.

[14] Dagotto E. Nanoscale phase separation and colossal magnetoresistance, Springer Series in Solid State Physics 136 (Springer, Berlin), 2003.

[15] Sarma D D, Topwal D and Manju U. Direct observation of large electronic domains with memory effect in doped manganites. Physical Review Letters, 2004; 93: 097202(1)–097202(4).

[16] Moreo A, Mayr M, Feiguin A, Yunoki S and Dagotto E. Giant cluster coexistence in doped manganites and other compounds. Physical Review Letters, 2000; 84: 5568–5571.

[17] Griffiths R B. Nonanalytic behavior above the critical point in a random Ising ferromagnet. Physical Review Letters, 1969; 23: 17–19.

[18] Woo H, Tyson T A, Croft M, Cheong S W and Woicik J C. Correlations between the magnetic and structural properties of Ca-doped $BiMnO_3$. Physical Review B, 2001; 63: 134412(1)–134412(12).

[19] Bokov V A, Grigoryan N A and Bryzhina M F. X-Ray diffraction and magnetic studies of solid solutions $Bi_{1-x}Ca_xMnO_3$. Physica Status Solidi, 1967; 20: 745–754.

[20] Bao W, Axe J D, Chen C H and Cheong S W. Impact of charge ordering on magnetic correlations in perovskite (Bi, Ca) MnO_3. Physical Review Letters, 1997; 78: 543–546.

[21] Banwell C N and McCash E M. Fundamental of molecular spectroscopy (Tata McGraw-Hill, 1997).

[22] Stevenson J W, Nasrallah M M, Anderson H U and Sparlin D M. Defect structure of $Y_{1-y}Ca_yMnO_3$ and $La_{1-y}Ca_yMnO_3$. Journal of Solid State Chemistry, 1993; 102: 175–184.

[23] Muller K A. Electron Paramagnetic Resonance of Manganese IV in $SrTiO_3$. Physical Review Letters, 1959; 2: 341.

[24] Muller K A, Berlinger W, Blazey K W and Albers J. Electron paramagnetic resonance of Mn^{4+} in $BaTiO_3$. Solid State Communications, 1987; 61: 21–25.

[25] Shengelaya A, Zhao G M, Keller H and Muller K A. EPR Evidence of Jahn-Teller polaron formation in $La_{1-x}Ca_xMnO_{3+y}$. Physical Review Letters, 1996; 77: 5296–5299.

[26] Gulley J E and Jacarrino V. Impure exchange-coupled paramagnets; Electron-Paramagnetic-Resonance Studies. Physical Review B, 1972; 6: 58–73.

[27] Oseroff B, Torikachvili M, Singley J and Ali S. Evidence for collective spin dynamics above the ordering temperature in $La_{1-x}Ca_xMnO_{3+\delta}$. Physical Review B, 1996; 53: 6521–6525.

[28] Causa M T, Tovar M, Caneiro A, Prado F, Ibanez G, Ramos C A, Butera A, Alascio B, Obradors X, Pinol S, Tokura Y and Oseroff S B. High-temperature spin dynamics in CMR manganites: ESR and magnetization. Physical Review B, 1998; 58: 3233–3239.

[29] Kumar A, Ghosh N, Joshi J P, Bhat H L and Bhat S V. Electron paramagnetic resonance studies of the insulating ferromagnetic manganite $Nd_{0.8}Pb_{0.2}MnO_3$ above the transition temperature. Solid State Communications, 2002; 123: 379–382.

[30] Anuradha K N, Rao S S and Bhat S V. EPR Evidence for premonitory charge-ordering fluctuations in hydrothermally grown $Pr_{0.57}Ca_{0.41}Ba_{0.02}MnO_3$ Nanowires. Applied Magnetic Resonance, 2009; 36: 347–356.

[31] Seehra M S. New method for measuring the static magnetic susceptibility by paramagnetic resonance. Review of Scientific Instruments, 1968; 39: 1044–1047.

[32] Ramos C A, Causa M T, Tovar M, Obradors X and Pinol S. Magnetization and FMR in $La_{0.7}Pb_{0.3}MnO_3$ single crystals. Journal of Magnetism and Magnetic Materials, 1998; 177–181: 867–868.

[33] Kurian J and Singh R. Electron spin resonance and resistivity studies of charge-ordered $Bi_{1-x}Sr_xMnO_3$. Journal of Alloys and Compounds, 2011; 509: 5127–5136.

[34] Ramesh A and Singh R. Effect of Pr doping on the properties of $Bi_{0.5-x}Pr_xCa_{0.5}MnO_3$ ($0 \le x \le 0.50$) manganites. Ceramics International, 2015; 41: 4759–4767.

[35] Oumezzine M, Pena O, Kallel S and Zemni S. Critical phenomena and estimation of the spontaneous magnetization through magnetic entropy change in $La_{0.67}Ba_{0.33}Mn_{0.98}Ti_{0.02}O_3$. Solid State Sciences, 2011; 13: 1829–1834.

[36] Banerjee S K. On a generalized approach to first and second order magnetic transitions, Physical Letters, 1964; 12: 16–17.

[37] Kim D, Revaz B, Zink B L, Hellman F, Rhyne J J and Mitchell J F. Tricritical point and the doping dependence of the order of the ferromagnetic phase transition of $La_{1-x}Ca_xMnO_3$. Physical Review Letters, 2002; 89: 227202(1)–227202(4).

[38] Panopoulos N, Koumoulis D, Diamantopoulos G, Belesi M, Fardis M, Pissas M, and Papavassiliou G. Spin order and lattice frustration in optimally doped manganites: A high-temperature NMR study. Physical Review B, 2010; 82: 235102(1)–235102(9).

[39] Adams C P, Lynn J W, Smolyaninova V N, Biswas A, Greene R L, Ratcliff II W, Cheong S-W, Mukovskii Y M and Shulyatev D A. First-order nature of the ferromagnetic phase transition in (La–Ca)MnO_3 near optimal doping. Physical Review B, 2004; 70: 134414(1)–134414(12).

[40] Ghosh K, Lobb C J, Greene R L, Karabashev S G, Shulyatev D A, Arsenov A A and Mukovskii Y. Critical phenomena in the double-exchange ferromagnet $La_{0.7}Sr_{0.3}MnO_3$. Physical Review Letters, 1998; 81: 4740–4743.

[41] Vijayan D, Kurian J and Singh R. ESR studies on $Bi_{0.5}Ca_{0.5}Mn_{0.95}TE_{0.05}O_3$ (TE = V, Cu, and Zn). IEEE Transaction on Magnetics, 2011; 47: 2701–2704.

[42] Vijayan D, Kurian J and Singh R. Electron spin resonance and magnetization studies on $Bi_{0.5}Ca_{0.5}Mn_{0.95}TM_{0.05}O_3$ (TM = Cr, Fe, Co and Ni). Journal of Applied Physics, 2012; 111: 07D716 (1)–07D716 (3).

[43] Kurian J and Singh R. Electron spin resonance studies of $Bi_{0.55}Ca_{0.45}MnO_3$ nanoparticles. Journal of Applied Physics, 2009; 105: 07D718(1)–07D718(3).

IntechOpen

IntechOpen